Modeling the mass and surface heat budgets in a coastal blue ice area of Adelie Land, Antarctica

Vincent Favier,[1] Cécile Agosta,[1] Christophe Genthon,[1] Laurent Arnaud,[1] Alexandre Trouvillez,[1,2] and Hubert Gallée[1]

Received 29 November 2010; revised 20 May 2011; accepted 1 June 2011; published 26 August 2011.

[1] Meteorological data recorded from 12 December 2008 to 30 June 2010 were analyzed to assess the surface energy balance (SEB) in a blue ice area of Cap Prudhomme, Adelie Land (66°41′S, 139°55′E). The SEB was computed with a newly developed model forced by direct measurements and with a voluntarily limited number of parameters to better assess model sensitivity. Incoming short-wave radiation was corrected for the slope and orientation of the local terrain assuming direct and diffuse radiation components. Turbulent heat fluxes were assessed using the bulk aerodynamic approach. Heat conduction in the ice was computed by solving the thermal diffusion equation. Snow accumulation was modeled using ERA interim total precipitation and a one-dimensional erosion model. The surface heat budget and accumulation/erosion model accurately reproduced field observations. The occurrence of blue ice is linked with higher rates of erosion than in the surrounding snow covered areas, which may be caused by local flow divergence or snow not being redistributed from higher elevations. Melting occurs between December and February when incoming short-wave radiation is high. However, the SEB was closely linked to air temperature through the incoming long-wave radiation and the turbulent sensible heat flux. Several warm events caused by cyclones intruding into the continent led to significant warming of the ice and high melting rates. Intruding cyclones were also associated with high precipitation that led to significant accumulation. Except in blue ice areas, modeling suggests that expected higher precipitation in a warmer climate will result in more accumulation.

Citation: Favier, V., C. Agosta, C. Genthon, L. Arnaud, A. Trouvillez, and H. Gallée (2011), Modeling the mass and surface heat budgets in a coastal blue ice area of Adelie Land, Antarctica, *J. Geophys. Res.*, *116*, F03017, doi:10.1029/2010JF001939.

1. Introduction

[2] As Antarctica is the main ice system on Earth, its future is an important issue for the scientific community. Because the Antarctica ice budget is currently slightly imbalanced, the increasing mass losses at its periphery in recent decades [e.g., *Rignot et al.*, 2008] have generated a major threat due to the impact on sea level rise. The Surface Mass Budget (SMB) is the only variable that could mitigate the sea level rise, but many questions remain concerning its current and future values. For instance, a slight increase in surface elevation has been observed in the interior of the continent, suggesting a recent mass gain [e.g., *Helsen et al.*, 2008], whereas Antarctic precipitation has not undergone any significant change since the 1950s [*Monaghan et al.*, 2006]. This contradiction points out the uncertainty of SMB measurements and interpretations. Long-term monitoring systems in the field are scarce at these latitudes [e.g., *Intergovernmental Panel on Climate Change*, 2007], and snow/ice ablation processes are rarely described [e.g., *Bintanja et al.*, 1997; *Genthon et al.*, 2007]. The lack of data makes it difficult to assess the accuracy of climatic modeling or remote sensing. In this context, developing programs to measure and model the Surface Energy Balance (SEB) [e.g., *Bintanja et al.*, 1997] and the SMB [e.g., *Eisen et al.*, 2008; *Agosta et al.*, 2011; *Gallée et al.*, 2011] is a crucial issue.

[3] The GLACIOCLIM-SAMBA observatory [e.g., *Genthon et al.*, 2007; *Agosta et al.*, 2011] was set up in Adelie Land with this aim in view. In the study area, blue ice (BI) often occurs close to the coast, reflecting local strong ablation conditions due to high snow erosion rates [e.g., *Genthon et al.*, 2007] caused by divergence in the katabatic wind field (e.g., on topographic protrusions), high sublimation [e.g., *Bintanja et al.*, 1997] of airborne crystals, and/or melt [e.g., *van den Broeke et al.*, 2006]. Despite the fact that BI only covers approximately 1% of the surface area of Antarctica, it has lower albedo, is generally a few degrees warmer in summer, and may be more sensitive to climate change than surrounding areas [e.g., *Bintanja*, 1999]. Only rare data are available on coastal BI areas where melting

[1]LGGE, UJF-CNRS, Saint Martin d'Hères, France.
[2]Cemagref, UR ETNA, Saint Martin d'Hères, France.

0148-0227/11/2010JF001939

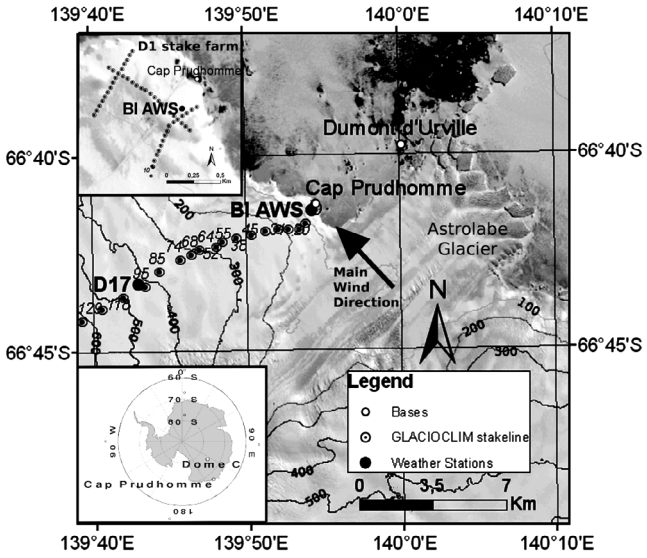

Figure 1. Orientation map showing the location of AWS and bases. The bottom left inset shows the location of Dome C and Cap Prudhomme bases in Antarctica. The top left inset is a zoom around BI AWS in the main map and shows the D1 stake farm. Elevation lines are from the digital elevation model of *Korona et al.* [2009], which was computed from SPOT5 images obtained during the fourth International Polar Year (2007–2009). The SPOT5 image is also included to show the Astrolabe Glacier.

occurs [e.g., *Genthon et al.*, 2007; *Rasmus*, 2009; *Hoffman et al.*, 2008]. The objective of this paper is to provide a careful characterization of accumulation and ablation processes in a BI area of Adelie Land using long-term (18 months) meteorological measurements and a complete SEB computation with accurate resolution of thermal diffusion in the ice and modeling of snow accumulation and erosion. This paper is an extension of [*Genthon et al.*, 2007], in which the snow model CROCUS was applied along with an original parameterization of blowing snow. Here we present a simpler model mainly forced by direct measurements and with a limited number of parameters with the aim of controlling model sensitivity.

[4] The paper is organized as follows: After a description of the regional climatic conditions in section 2, we describe the data and methods used in section 3. In section 4, we examine the ablation processes, results and uncertainties. Section 5 includes a discussion on local BI ablation processes and our conclusions.

2. Climatic Setting

[5] Cap Prudhomme (CP, 66.69°S, 139.90°E, 30 m above sea level (asl), Figure 1) hosts a summer station at the departure point of the logistical traverse from the coast to the French-Italian Concordia station located ~1100 km inland at Dome C (DC) on the plateau. The CP station is located 5 km away from the permanent French station in Adelie Land, Dumont D'Urville, for which the mean meteorological conditions are reported by *König-Langlo et al.* [1998]. Like solar radiation influx, temperatures follow a strong seasonal cycle (Figure 2), which has major consequences for accumulation/ablation processes [e.g., *Genthon et al.*, 2007]. With a mean temperature of −10.8°C, cold conditions mean that precipitation is mainly solid and that melting only occurs during the summer months (December to February). The coast of Adelie Land is located just south of the Sub-Antarctic Convergence and is affected by frequent low-pressure systems coming from the northwest [e.g., *King and Turner*, 1997]. Cloudiness does not present a clear seasonal cycle [e.g., *King and Turner*, 1997] and precipitation occurs year round [*König-Langlo et al.*, 1998]. Only a few rare cases of drizzle and rainfall have been reported [*König-Langlo et al.*, 1998]. Along the coast, precipitation is mainly due to cyclones that intrude into the continent and adiabatically cool as they rise with the topography.

[6] Two main climate characteristics in the area are the sloped temperature inversion and negative buoyancy forces that are responsible for relatively strong and persistent katabatic winds [*Gallée and Pettré*, 1998; *König-Langlo et al.*, 1998]. The pattern of heating and cooling at the Earth's surface strongly controls wind circulation, which is consequently stronger in winter. Since the Coriolis acceleration affects the

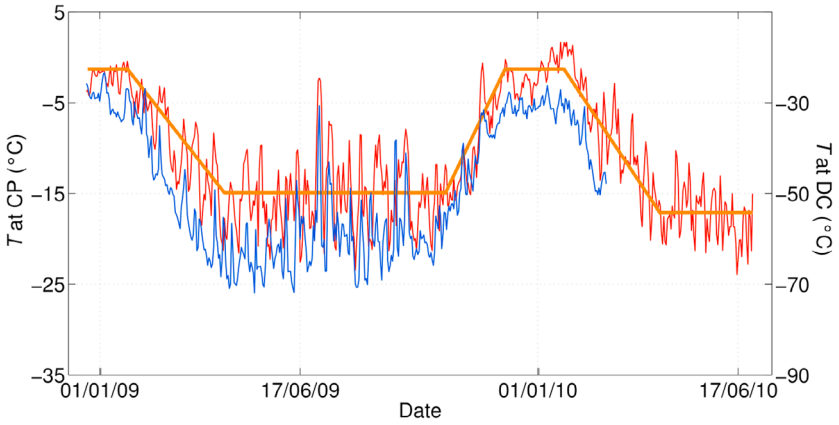

Figure 2. Daily air temperature at a height of 2 m (red line) and fitted temperature trends (thick orange lines) at BI-AWS. Also shown is daily air temperature at a height of 2 m at Dome C (thin blue line).

Table 1. List of Equipment Sensors With Their Specificity, Installed at BI-AWS and at D17

Quantity[a]	Type of Sensor	Height[b] (cm)	Accuracy (s) According to the Manufacturer
Air temperature	Vaisala HMP 45, aspirated[c]	200	±0.4°C
Relative humidity	Vaisala HMP 45, aspirated[c]	200	±3%
Wind speed	Young 05103	210	±0.3 m s^{-1}
Wind direction	Young 05103	210	±3°
Incident short-wave radiation	Kipp and Zonen CM3[d], $0.305 < \lambda < 2.8$ μm	85	±5%[e]
Reflected short-wave radiation	Kipp and Zonen CM3[d], $0.305 < \lambda < 2.8$ μm	85	±5%[e]
Incoming long-wave radiation	Kipp and Zonen CG3[d], $5 < \lambda < 50$ μm	85	±5%[e]
Outgoing long-wave radiation	Kipp and Zonen CG3[d], $5 < \lambda < 50$ μm	85	±5%[e]
Ice temperature	PT100 temperature probes[d]	−60, −160, −410, −910	±0.3°C
Surface elevation	Campbell acoustic gauge, SR50A	160	±1 cm

[a]Quantities are recorded as half-hourly means over 10 s time intervals except for wind direction, which is an instantaneous value measured at 30 min intervals.
[b]Heights are variable but known with reasonable accuracy in summer thanks to manual measurements made at 10 day intervals, and sensor height is corrected assuming acoustic gauge measurements made during the rest of the year.
[c]To prevent measurement errors due to radiation, Vaisala thermohygrometers are adequately shielded.
[d]Sensors that were only present at BI-AWS.
[e]Accuracy for daily totals.

northward katabatic flow, a mean southeasterly wind drift (Figure 1) is observed all year round at Dumont d'Urville [*König-Langlo et al.*, 1998].

3. Data

3.1. Meteorological Measurements

[7] In this paper we use the meteorological data recorded by two meteorological stations (Table 1): (1) an automated weather station (AWS) set up on the blue ice (BI-AWS) (66.69°S, 139.90°E, 64 m asl) from 12 December 2007 to 30 June 2010 (the station was located 150 m from the sea and was specifically designed to measure the surface heat budget, and ice temperature down to a depth of 9 m; radiation and ice temperature were measured after 12 December 2008 and 4 February 2009, respectively); and (2) an AWS located at D17 (66.72°S, 139.72°E, 426 m asl, 10 km inland), along the traverse to Dome C in a positive net accumulation area. Data were available from 18 December 2008 to 24 February 2010.

[8] The sensor characteristics are listed in Table 1. Precipitation is not recorded at Cap Prudhomme because high wind speeds prevent accurate measurement in this harsh environment. Thus, the ECMWF ERA-Interim [*Simmons et al.*, 2006] precipitation data from the grid point (66°S, 140°E) located closest to Cap Prudhomme was used. ERA-Interim nominal horizontal resolution is ~40 km (T256 spectral truncation). In this paper, we also used data from a grid point located slightly inland (67.5°S, 140°E).

[9] Finally, we used unaspirated air temperature data recorded at a height of 2 m by an AWS located close to Dome C station (75.1°S, 123.3°E, 3233 m asl) from 11 December 2008 to 27 February 2010.

3.2. Ablation Measurements

[10] Accumulation and ablation were assessed from stake measurements made by the GLACIOCLIM-SAMBA (SurfAce Mass Balance of Antarctica) stake network (Figure 1) [e.g., *Genthon et al.*, 2007; *Agosta et al.*, 2011]. Ablation is monitored at Cap Prudhomme station at a stake farm (labeled "D1 stake farm" in Figure 1) with 48 ablation polycarbonate stakes that are measured monthly. The BI-AWS is located in the northern (lower elevation) part of the D1 network where BI is almost permanent, whereas stakes located in the upper (Southern) part present zero net accumulation. The mean mass balance for the D1 stake farm was assessed by empirical orthogonal function (EOF) analysis of data from the 48 stakes as described by *Genthon et al.* [2007]. This allows the mean accumulation/ablation pattern to be described at a larger spatial scale.

[11] In addition, continuous surface level measurements were made by acoustic depth gauges (SR50) at BI-AWS and at D17, yielding information on snow accumulation and snow/ice ablation. At D17, data were available from 18 December 2008 to 24 February 2010. At BI-AWS, data were available from 7 February 2009 to 30 June 2010. SR50 data were smoothed considering a 3 h running mean of maximum SR50 data recorded at 30 min intervals. Snow depth is the difference between SR50 measurement at time t and the maximum SR50 value observed before t.

[12] At BI-AWS, the stakes located closest to BI-AWS (stakes 6-I, 7-VII and 8-VII) revealed very low snow accumulation during the study period, and showed the same elevation pattern as that observed at BI-AWS, enabling us to compensate for gaps in the data. On 20 November 2009, the acoustic depth gauge membrane was damaged by the wind, and the sensor membrane was replaced on 18 December 2009 (without moving the sensor structure). In addition, data from 24 December 2009 to 12 January 2010 were discarded because comparison with the surrounding stakes showed that the SR50 mast was sinking into the ice. The ablation observed on stakes 6-I, 7-VII and 8-VII was used to fill this data gap.

[13] The snow density value is required to retrieve the equivalent water content of the accumulated snow. Snow density was not systematically evaluated during field measurements. However, wind speed is almost continuously high and snow density quickly increases to ρ_{snow} = 350 kg m^{-3} after snowfall [e.g., *Genthon et al.*, 2007]. Ice density was evaluated using a short surface ice core sampled close to

BI-AWS on 29 December 2009, which revealed a constant density of $\rho_{ice} = 850$ kg m$^{-3} \pm 20$ kg m^{-3} between the surface and a depth of 4 m.

3.3. Surface Energy Balance Computation

[14] The incoming energy in the ice ($F_{surface}$) can be computed as follows [e.g., *Oke*, 1987]:

$$S_{\downarrow} - S_{\uparrow} + L_{\downarrow} - \left[(1-\varepsilon)L_{\downarrow} + \varepsilon\sigma T_s^4\right] + \mathrm{LE} + H = F_{surface}\left(\text{in W m}^{-2}\right) \quad (1)$$

where $S_{\downarrow}$ is incoming solar radiation, $S_{\uparrow}$ is reflected short-wave radiation ($S = S_{\downarrow} - S_{\uparrow}$ is net short-wave radiation), $L_{\downarrow}$ is incoming long-wave radiation and the term in parentheses is outgoing long-wave radiation $L_{\uparrow}$ measured in the field ($R = S + L_{\downarrow} - L_{\uparrow}$ is the net radiation). $\varepsilon = 0.99$ is surface emissivity, $\sigma = 5.67\ 10^{-8}$ W m^{-2} K^{-4} is the Stefan-Boltzmann constant, T_s is surface temperature, H and LE are turbulent sensible and latent heat fluxes, respectively. The fluxes toward the surface are positive. The heat flux supplied by precipitation was not taken into account because precipitation intensity is low.

[15] $F_{surface}$ is the energy available at the surface. Part of the short-wave radiation is actually not available for the warming/cooling processes at the surface or for melting because the short-wave flux partly penetrates the ice [e.g., *Bintanja et al.*, 1997]. Hence, $F_{surface}$ is separated into two terms:

$$F_{surface} = G_0 + (1-a)S\left(\text{in W m}^{-2}\right) \quad (2)$$

where G_0 is energy excess or deficit at the surface. In equation (2), a is the fraction of short-wave radiation that is absorbed in the top layer of the model (at the surface). When the surface temperature is 0°C, the positive G_0 values represent the energy available for melting (G_0 is then initialized to zero before computing equation (16)). Otherwise, this amount is used to cool/warm the frozen surface and underlying snow/ice (section 3.8).

3.4. Radiation Measurements

[16] The four terms of the radiation balance were measured in the field with a Kipp and Zonen net radiometer (Table 1). Although *Obleitner and de Wolde* [1999] suggested applying a systematic correction to the measurements of long-wave radiations in relation to incident solar radiation, we did not do so because the surface temperature derived from outgoing long-wave radiation was in better agreement with observed surface melt conditions during field trips without this correction than with it. For model validation, the measured surface temperature was obtained from $L\uparrow$ values using the Stefan-Boltzmann equation.

3.5. Incoming Short-Wave Radiation Over a Sloping Terrain

[17] For easier control of sensor orientation, the radiation sensors were installed in a horizontal plane, whereas in reality, the surface presents a significant slope (the average site slope is 10°). In this configuration, the net short-wave radiation budget has to be estimated on a sloping terrain using geometrical calculations [e.g., *Favier et al.*, 2004]. This calculation allows computation of a ratio (hereafter referred to as $R_{slope/h}$) between the radiation received under a direct beam by a sloping surface and the radiation received by a horizontal surface. Because diffuse and direct incoming short wave radiations do not hit the surface at the same angle of incidence, both components have to be estimated. For this task, we first modeled theoretical direct S_n and diffuse S_d components under clear sky conditions. Comparing $S_n + S_d$ with measured $S_{\downarrow}$ gave the attenuation of incoming solar radiation by clouds, from which we deduced the direct S'_n and diffuse S'_d components under overcast conditions. Computation is described in detail below.

[18] Clear sky short-wave radiation was estimated according to the SOLTRAN model described by *Bird and Hulstrom* [1981]. Despite its simplicity, this model (also known as Iqbal's model [*Iqbal*, 1983]), gives good results [e.g., *Corripio*, 2003] as also shown in a review by *Niemelä et al.* [2001] in which several models were compared. In the SOLTRAN model, atmospheric turbidities [e.g., *Ångström*, 1961] at 0.38 μm and 0.5 μm wavelengths are needed to compute diffusion by aerosols [*Bird and Hulstrom*, 1981], and we used values measured during the IAGO project at D47 (located 100 km from our study site) [*Wendler and Ishikawa*, 1988]. We assumed the solar constant was equal to 1368 W m^{-2}. *Bourges* [1985] provided the solar declination values. The model of *Bird and Hulstrom* [1981] correctly described clear sky conditions at our study site (data not shown).

[19] For overcast conditions, we assumed that the diffuse short-wave (S'_d) component of the total short-wave radiation balance linearly decreases according to $S_{\downarrow}/(S_n + S_d)$ values. Overcast conditions corresponding to purely diffuse radiation were assumed when $S_{\downarrow}/(S_n + S_d) \leq 0.175$. This condition is almost equivalent to saying: $S_{\downarrow}/S_{TOA} < 0.15$ [*Hock and Holmgren*, 2005], where S_{TOA} is incoming short-wave radiation at the top of the atmosphere. Under partially overcast conditions, direct and diffuse short-wave radiation is computed with the following linear interpolation:

$$S_{\downarrow} > 0.175(S_n + S_d) \Rightarrow S'_d = \left(\frac{S_d\left(\frac{S_{\downarrow}}{S_n + S_d} - 0.175\right) + S_{\downarrow}\left(1 - \frac{S_{\downarrow}}{S_n + S_d}\right)}{1 - 0.175}\right) \quad (3)$$

$$S_{\downarrow} \leq 0.175\ (S_n + S_d) \Rightarrow S'_d = S_{\downarrow} \quad (4)$$

Conservation of $S_{\downarrow}$ values is obtained with the following relation:

$$S'_n = S_{\downarrow} - S'_d \quad (5)$$

The incoming short-wave radiation over a sloping area is then deduced as follows:

$$S_{slope} = S'_n R_{slope/h} + S'_d \quad (6)$$

3.6. Turbulent Fluxes

[20] The turbulent heat fluxes are calculated using the bulk aerodynamic approach, including stability correction. This method has been already tested, validated and described

in numerous studies [e.g., *Denby and Greuell*, 2000; *Favier et al.*, 2004]. In this approach, a constant gradient is assumed between the level of measurement and the surface and consequently, surface values have to be evaluated. The stability of the surface layer is described by the bulk Richardson number Ri_b, which links the relative effects of buoyancy to mechanical forces [e.g., *Oke*, 1987]:

$$Ri_b = \frac{g(T - T_s)(z - z_{0m})}{Tu^2} \quad (7)$$

where T and u are mean values of air temperature (in K) and horizontal wind speed (in m s^{-1}) at the level of measurement z, respectively. The parameter g is acceleration of gravity (g = 9.81 m s^{-2}), and z_{0m} is the surface roughness parameter for momentum (in m). Assuming that local gradients of mean horizontal wind speed u, mean temperature T and mean specific humidity q are equal to the finite differences between the level of measurement and the surface, it is possible to give analytical expressions for the turbulent fluxes [e.g., *Oke*, 1987]:

$$\tau = \rho_a u^{*2} = \rho_a \frac{(ku)^2}{(\ln z/z_{0m})^2}(\Phi_m)^{-2} \ \left(\text{in kg m}^{-1}\ \text{s}^{-2}\right) \quad (8)$$

$$H = \rho_a \frac{C_p k^2 u(T - T_s)}{(\ln z/z_{0m})(\ln z/z_{0T})}(\Phi_m \Phi_v)^{-1} \ \left(\text{in W m}^{-2}\right) \quad (9)$$

$$LE = \rho_a \frac{L_s k^2 u(q - q_s)}{(\ln z/z_{0m})(\ln z/z_{0q})}(\Phi_m \Phi_v)^{-1} \ \left(\text{in W m}^{-2}\right) \quad (10)$$

where q_s is mean specific humidity at the surface (in g kg^{-1}), $\rho_a = P_{atm}/R_a T$ (in kg m^{-3}, R_a being the specific gas constant for dry air) is air density at Cap Prudhomme station (where P_{atm} is around 980 hPa), C_P is specific heat capacity for air at constant pressure ($C_p = C_{pd}$ (1 + 0.84q) with C_{pd} = 1005 J kg^{-1} K^{-1} is specific heat capacity for dry air at constant pressure), L_s is latent heat of sublimation of snow or ice (L_s = 2.834 10^6 J kg^{-1}), and k is the von Karman constant (k = 0.4). τ is surface stress and u^* is the friction velocity (in m s^{-1}); z_{0T} and z_{0q} are the surface roughness parameters for temperature and humidity, respectively. To compute turbulent fluxes (equations (8), (9) and (10)), it is assumed that the air temperature is equal to the surface temperature of the snow/ice at z_{0T} and that the air is saturated with respect to the surface temperature of the snow/ice at z_{0q}. This last assumption helps calculate surface specific humidity q_s.

[21] The nondimensional stability functions for momentum (Φ_m), heat (Φ_h) and moisture (Φ_v) can be expressed in terms of Ri_b:

For Ri_b positive (stable)

$$(\Phi_m \Phi_h)^{-1} = (\Phi_m \Phi_v)^{-1} = (1 - 5Ri_b)^2 \quad (11)$$

For Ri_b negative (unstable)

$$(\Phi_m \Phi_h)^{-1} = (\Phi_m \Phi_v)^{-1} = (1 - 16Ri_b)^{0.75} \quad (12)$$

The bulk method was applied between the surface and the level of measurement of T, q and u. To apply the bulk aerodynamic approach to the measurements, T_s was obtained by modeling ice temperature (see section 3.8.). Attribution of the actual roughness length at the site was obtained from calibration with direct sublimation measurements. Since u was not measured at exactly the same elevation (a difference of 10 cm) to prevent perturbations caused by the AWS mast, the wind speed was recalculated at the level of T and q assuming that the vertical wind speed profile is logarithmic (neutral conditions): $u = (u^*/k) \ln (z/z_{0m})$ with u^* defined by equation (8).

[22] We also defined the characteristic scales of potential temperature and of specific humidity by

$$\theta^* = \mathrm{H}/\left(\rho C_p u^*\right)(\text{in K}) \quad (13)$$

$$q^* = \mathrm{LE}/\left(\rho L_s u^*\right)\left(\text{in g kg}^{-1}\right) \quad (14)$$

Although the thermohygrometers were not aspirated, *Georges and Kaser* [2002] showed that the impact of errors in the measurement of temperature and relative humidity on turbulent heat flux computation is negligible when wind speed exceeds 3 m s^{-1}. Moreover, at Cap Prudhomme, comparison of artificially aspirated and nonaspirated thermohygrometers showed that temperature and relative humidity bias in summer is less than 0.5°C and 3% if the wind speed is higher than 3 m s^{-1}. Turbulent heat fluxes are not negligible when the wind speed is less than 3 m s^{-1}. However, a nonnegligible impact due to the combination of low wind speed (u < 3 m s^{-1}) and high radiation (e.g., $S_\downarrow$ > 700 W m^{-2}) is rare (1.5% of events during the study period).

3.7. Roughness Parameters

[23] Turbulent heat fluxes are very sensitive to the choice of surface roughness lengths z_{0m}, z_{0q} and z_{0T}. The ratio between roughness lengths (z_{0m}/z_{0q} and z_{0m}/z_{0T}) depends on the Reynolds number of the flow according to *Andreas* [1987] polynomials. For high Reynolds numbers (aerodynamically rough flows), we assumed polynomials suggested by *Smeets and van den Broeke* [2008] for hummocks. The roughness lengths for various surfaces have already been studied for BI and snow [e.g., *van den Broeke et al.*, 2005]. At Cap Prudhomme station, *Genthon et al.* [2007] assumed z_{0m} = 0.16 mm for snow. However, the roughness length for ice required more attention as described hereafter.

[24] During the two summers concerned, small penitents (of 6–8 cm in height) were observed. The roughness length of the ice penitent surfaces was assessed from direct sublimation measurements with four lysimeters [e.g., *Favier et al.*, 2004]. Direct measurements of sublimation were made three times a day for 25 days during the 08–09 season and 30 days during the 2009–2010 season. The roughness length was assumed to be constant despite variations in the height of the surface penitents. For these calibrations, the surface temperature was derived from the outgoing longwave radiation $L_\uparrow$ using the Stefan-Boltzmann equation. Optimization was performed on z_{0m} to minimize the difference between total computed and measured sublimation (Figure 3). Calibration led to roughness length values of

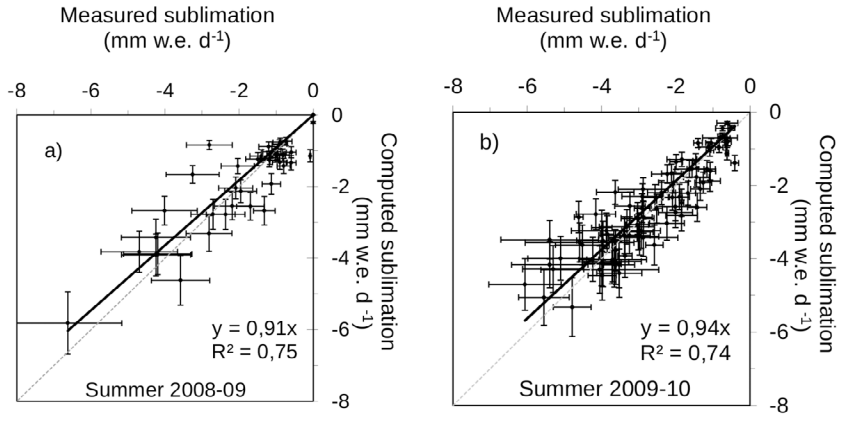

Figure 3. Comparison of measured and computed sublimation (a) between 22 December 2008 and 8 January 2009 with z_{0m} = 0.49 mm and (b) between 16 December 2009 and 25 January 2010 with z_{0m} = 5.2 mm.

z_{0m} = 0.49 mm in 2008–2009 and z_{0m} = 5.2 mm in 2009–2010. For the entire period of study, we assumed a mean value of z_{0m} = 2.85 mm. However, note that the local topography may impact winds and turbulence because wind generally flows over the sea/sea ice before hitting an ice cliff and then BI-AWS (Figure 1). Calibration may be affected by this and extrapolating z_{0m} value to other locations should be done with caution.

3.8. Thermal Diffusion in the Snow/Ice

[25] Assuming horizontal homogeneity, temperature distribution inside the ice is governed by the thermodynamic energy equation [*Bintanja et al.*, 1997; *Picard et al.*, 2009]:

$$\rho C_{p-ice}\frac{\partial T(z,t)}{\partial t} = -K_s\frac{\partial^2 T(z,t)}{\partial z^2} + \frac{\partial S_i(z,t)}{\partial z} \qquad (15)$$

where z is coordinate normal to the surface (positive downward), ρ is snow density (ρ_{snow} = 350 kg m^{-3}) or ice density (ρ_{ice} = 850 kg m^{-3}), T(z) is ice temperature at depth z, K_s is thermal conductivity, $C_{p\text{-}ice}$ is specific heat capacity of ice at constant pressure, which depends on temperature ($C_{p\text{-}ice}$(z) = 185 + 7.037 T(z) [*Dorsey*, 1940]), and $S_i(z) = S(1-a)\,e^{-bz}$ is penetrated short-wave flux at depth z. *Bintanja et al.* [1997] suggest that a is 0.8 for BI, but different values for a were tested to optimize heat storage in the ice according to temperature measurements. The best fit was observed with a_{ice} = 0.61. Because snow was not persistent, a meticulous calibration of a_{snow} for snow was difficult at the study site and we assumed that a_{snow} = 0.90, as suggested by *Bintanja and van den Broeke* [1995]. However, the model is almost insensitive to this parameter. Below the surface, the short-wave flux decreases exponentially with a constant extinction coefficient b = 2.5 m^{-1} [*Bintanja et al.*, 1997]. Distinct thermal conductivity was used for ice ($K_{s\text{-}ice}$ = 2.0715 W m^{-1} K^{-1}) and snow ($K_{s\text{-}snow}$ = 0.39 W m^{-1} K^{-1}). $K_{s\text{-}snow}$ was computed according to *Douville et al.* [1995], as a function of snow density.

[26] Thermal diffusion was computed according to an explicit scheme to a depth of 18.2 m, with a 2 cm grid resolution and a 20 s time step. The Neumann boundary condition was assumed at the surface [e.g., *Picard et al.*, 2009]:

$$K_s\frac{\partial T(z,t)}{\partial z} = -G_0 \qquad (16)$$

[27] The Neumann boundary condition was also used at the bottom of the grid. The best fit between measured and modeled ice temperature at 910 cm was obtained when the basal heat flux G_s = −0.4 W m^{-2}. This value is high, but the model is only poorly sensitive to this parameter.

[28] The initial temperature profile on 14 December 2008 was deduced from ice temperature measurements made on 14 December 2009. A linear interpolation was assumed between each level (at the surface and at depths of 60 cm, 160 cm, 410 cm and 910 cm). Between 4 February 2009 and 4 December 2008 (date the thermometers were installed), the surface already presented significant ablation (about 20 cm). Thus, the surface reference level on 14 December 2009 was 20 cm higher than on 4 February.

3.9. Snow Accumulation and Ablation

[29] The short-wave radiation budget and heat conduction are strongly affected if snow accumulates at the surface. Accumulation was obtained assuming precipitation (P) from the ECMWF ERA interim reanalysis at 140°E and 66°S and an erosion model based on *Genthon et al.* [2007], whose approach is a simplification of the model of *Gallée et al.* [2001] to fit a one-dimensional problem. Snow precipitation at 0000 and 1200 UT is the result of forecasts at 1200 and 0000 UT, respectively. Data were corrected for a sloping terrain. Snow density was assumed to be constant. A new mesh was included in the grid when the increase in snow depth exceeded the size of one grid element (2 cm). The temperature of the new grid nodes was equal to the computed surface temperature at the previous time step. When ablation exceeded the size of one grid element, one layer was removed from the surface and the computed surface temperature was applied to the new uppermost layer.

[30] Here, *Genthon et al.* [2007] equations for erosion were adapted to account for sedimentation flux and recycling of

Table 2. Model Results of the Reference Run[a]

Parameter	Value
Measured mass balance (mm w.e.)	−562
Modeled mass balance (mm w.e.)	−586
Mean T_s difference[b] (°C)	−0.14
Mean T_s standard deviavion (°C)	0.82

[a]Mean differences and standard deviations of modeled surface temperature errors are also shown.
[b]Negative value indicates that the modeled surface temperature is lower than the observed temperature.

snow in order to schematically represent effects of flow divergence or convergence. We initially assumed equation (6) of *Genthon et al.* [2007] that we corrected as follows:

$$E_p = C\,u^{*0.73}\left(u^{*2} - u_t^{*2}\right) \tag{17}$$

where E_p is potential erosion flux, u_t^* = 0.3 m s^{-1} is threshold friction velocity and C = 0.1 (as a gross evaluation [*Genthon et al.*, 2007]). Assuming that there is almost a balance between deposited and remobilized drifting snow [*Gallée et al.*, 2001], we write

$$E_{net} = E_p - D \approx 0 \tag{18}$$

where E_{net} is net erosion and D is sedimentation flux. We assumed that differences between E_p and D express the convergence and/or divergence of airflow. Since wind direction is almost constant in the field, we assumed that this difference can be expressed by including a constant parameter (R_{cyc}) as follows:

$$D = R_{cyc}E_p \tag{19}$$

R_{cyc} = 1 means that erosion is exactly compensated by sedimentation, corresponding to characteristics observed if the flux neither converges nor diverges. The more the flux diverges, the lower the value of the R_{cyc} parameter. Retrieving surface elevation requires calibration of the R_{cyc} parameter, which also depends on ρ_{snow}.

3.10. Correction of Reflected Short-Wave Radiation

[31] The SEB was computed considering $S_\uparrow$ measurements. However, the model often suggested that snow was present at the surface, whereas direct observation by SR50 and albedo measurements indicated that the ice was uncovered. Applying $S_\uparrow$ measurements would artificially force the model to follow field observations. In this case, we modeled $S_\uparrow$ assuming a "theoretical" snow albedo (hereafter referred to as α_{snow} = 0.81). This albedo value was deduced from local albedo measurements at 1200 LT (local time), and is in good agreement with measurements made at Dome C [*Pirazzini*, 2004] and with remote sensing data available along the traverse close to Cap Prudhomme, which suggested that albedo values of old snow would be close to 0.80 [*Gallet*, 2010, p. 109]. Corrections of $S_\uparrow$ were also performed when the model and observations did not agree in indicating uncovered ice. In this case, a mean theoretical ice albedo (hereafter referred to as α_{ice} = 0.6) was assumed to compute $S_\uparrow$. This value was deduced from summer albedo measurements at noon at the BI-AWS and is similar to albedo measurements made in other BI areas [e.g., *Reijmer et al.*, 2001].

[32] These assumptions suggest that when the snow cover (timing) is perfectly modeled, the SEB is computed with $S_\uparrow$ measurements only. Hence, if snow accumulation/ablation is deduced from SR50 observation, then $S_\uparrow$ does not require correction.

3.11. Model Calibration

[33] The model mainly depends on two parameters (R_{cyc} and a_{ice}), the other parameters mostly being justified by field measurements or having a low impact on energy and mass balances (see section 4.1). Because it is crucial to assess a_{ice} independently from R_{cyc}, a_{ice} was first calibrated by turning off the snow accumulation/erosion model and considering the snow cover obtained from SR50 acoustic depth gauge measurements. The parameter a_{ice} was calibrated to minimize errors in ice and surface temperatures. Next, snow accumulation was turned on using ERA-Interim precipitation and erosion modeling. R_{cyc} was estimated so that the mass balance was correctly reproduced. R_{cyc} = 0.9975 allowed good modeling of mass balance at BI AWS. We did not calibrate R_{cyc} to obtain the exact measured accumulated mass balance value at the end of the study period, but we paid close attention to reproducing mass balance variations. Results of reference modeling are presented in Table 2.

4. Results

4.1. Model Sensitivity

[34] The sensitivity of the model was examined assuming the measurement uncertainties specified by the manufacturer (Table 1). First, we tested the impact of each input variable (i.e., T, R_h (the specific humidity of the atmosphere at 2 m), $S_\downarrow$, $S_\uparrow$, $L_\downarrow$, u) uncertainty considering a systematic positive (or negative) deviation corresponding to the sensor accuracy provided by the manufacturer. Moreover, simulations were performed assuming 10 and 20% higher (lower) precipitation values than those provided by ERA-Interim. Finally, 1000 simulations were performed assuming that each input variable presents a random uncertainty. Random values followed a normal distribution with a zero mean, the standard deviation being equal to the sensor accuracy provided by the manufacturer. Results are presented in Table 3.

[35] The surface temperature and the surface mass balance sensitivities to each variable differ. Indeed, since the summer surface temperature presents a maximum of 0°C, positive SEB in summer has no impact on the surface temperature under melting conditions. On the other hand, snowmelt is closely related to this 0°C threshold, and an increase in the SEB during summer has a major impact on the surface mass balance. Hence, modeling the surface temperature is very sensitive to any variable that greatly increases the surface heat budget during winter and during the intermediate seasons (such as $L_\downarrow$ and H), whereas the surface mass balance is more sensitive to higher $S_\downarrow$ values. The strong dependence of mass balance on $S_\uparrow$ uncertainties demonstrates that BI melt is closely linked to surface albedo. Finally, $L_\downarrow$ impacts the surface heat budget all year round, which is clearly a crucial point of the SEB in this area. Indeed, because shortwave radiation influx is low, increasing cloudiness results in a more positive surface heat budget due to the increase in

Table 3. Model Sensitivity Tests on Input Variable Accuracy Performed at BI-AWS Between 12 December 2008 and 30 June 2010[a]

Sensor Uncertainty	T	R_h	$S\downarrow$	$S\uparrow$	$L\downarrow$	u	Random	P
Mean Surface T Difference (°C)								
$-2s$	−0.29	−0.08	−0.16	0.09	−0.39	−0.01	−0.01	0.07
$-1s$	−0.15	−0.04	−0.08	0.05	−0.18	0.00		0.03
$1s$	0.14	0.04	0.07	−0.05	0.18	0.00		−0.05
$2s$	0.29	0.08	0.14	−0.10	0.36	0.01		−0.05
Standard Deviation Ratio								
$-2s$	1.000	0.994	1.040	1.032	1.219	1.007	1.07	0.837
$-1s$	1.000	0.999	1.005	1.011	1.065	1.003		0.941
$1s$	1.004	1.002	1.014	1.000	0.952	0.998		1.099
$2s$	1.009	1.002	1.044	1.015	0.927	0.994		1.104
Mass Balance Difference (mm w.e.)								
$-2s$	49	−13	116	−80	92	1	−15	−27
$-1s$	21	−6	60	−39	42	0		−13
$1s$	−22	6	−64	38	−45	−1		14
$2s$	−47	11	−130	73	−92	−1		39

[a]Mean surface temperature and mass balance differences are presented for four cases assuming a constant error of $2s$, $1s$, $-1s$ and $-2s$, where s is the sensor uncertainty specified by the manufacturer (Table 1). The standard deviation ratio is the ratio of the standard deviation of surface temperature modeling errors of the study to that of the reference run. Random means that every measurement has a random error presenting a normal distribution with a zero mean and a standard deviation of $1s$.

incoming long-wave radiation (conditions of the so-called radiation paradox [*Ambach*, 1974]). Obtaining accurate radiation and temperature measurements at the study site is crucial. However, modeling results are much less sensitive to relative air humidity and almost not sensitive to wind speed. In fact, wind speed values are high and largely exceed ±0.3 m s^{-1}.

[36] Sensitivity tests with randomly distributed measurement uncertainties suggest that the model errors on T_s are centered and that T_s standard deviation differs only slightly (about 7%) from the reference run. However, we observed that the mass balance tends to be more negative if sensor uncertainties are included, because model sensitivity to meteorological inputs (T, $S_\downarrow$, $S_\uparrow$ and $L_\downarrow$) is not symmetrically distributed around 0.

[37] In the second step, we performed several runs to measure model sensitivity to each parameter. The parameters tested and results are listed in Table 4. At BI-AWS, different parameters are crucial for SEB modeling but fortunately these could be deduced from field data or from other studies and were consequently known. This includes the roughness lengths $z_{0m\text{-}snow}$ and $z_{0m\text{-}ice}$. For instance, low $z_{0m\text{-}snow}$ values produce considerable feedback that causes snow to accumulate, because this parameter also affects erosion. The mean measured slope and orientation are also crucial and the high sensitivity of the model to these parameters indicates that melting areas greatly depend on the characteristics of the local terrain. ε is expected to be important, because it influences estimated surface temperature (measurement) and surface temperature modeling. However, it only slightly affects temperature modeling. The model only weakly depends on the α_{snow} value because the surface snow cover is not permanent. We observed that model dependence increases when ρ_{snow} tends to 450 kg m^{-3}. The parameter ρ_{snow} finds

Table 4. Model Sensitivity Tests on Parameter Values at BI-AWS Between 12 December 2008 and 30 June 2010

	ε	G_s (W m^{-2})	a_{ice}	$K_{s\text{-}ice}$ (W m^{-1} K^{-1})	ρ_{ice} (kg m^{-3})	α_{ice}	$z_{0m\text{-}ice}$ (mm)	R_{cyc}	Slope	Azimuth	a_{snow}	$K_{s\text{-}snow}$ (W m^{-1} K^{-1})^2	ρ_{snow} (kg m^{-3})	α_{snow}	$z_{0m\text{-}snow}$ (mm)
Case 1	1.00	−0.04	0.59	1.9715	800	0.55	0.489	0.9955	8°	125°	0.88	0.29	250	0.76	0.006
Case 2	0.98	−4	0.63	2.0215	900	0.65	5.2	0.9985	12°	165°	0.92	0.49	400	0.86	0.06
Case 1 mean T_s difference (°C)	0.11	−0.00	0.01	−0.01	−0.01	0.00	−0.03	0.11	−0.06	−0.08	0.00	−0.01	0.08	0.06	−0.18
Case 2 mean T_s difference (°C)	−0.11	0.01	0.00	0.00	0.01	0.00	0.01	−0.09	0.05	0.04	0.00	0.00	−0.05	−0.07	0.16
Case 1 T standard deviation ratio	1.01	1.00	1.00	1.00	1.00	1.00	0.99	0.83	1.00	1.07	1.00	1.05	0.85	0.96	1.27
Case 2 T standard deviation ratio	1.00	1.00	1.00	1.00	1.00	1.00	1.01	1.10	1.03	1.00	1.00	0.96	1.06	1.13	0.77
Case 1 mass balance (mm w.e.)	5	0	23	0	0	0	15	−34	30	59	0	0	−27	−4	57
Case 2 mass balance (mm w.e.)	−5	−1	−24	0	0	0	−7	56	−30	−49	0	0	39	8	−51

[a]Mean surface temperature and mass balance differences in temperature and mean mass balance differences are shown for two cases (Case 1 & Case 2). The standard deviation ratio is the ratio of the standard deviation of surface temperature modeling errors of the study to that of the reference run. Parameter values for cases 1 and 2 are presented under the parameter name.

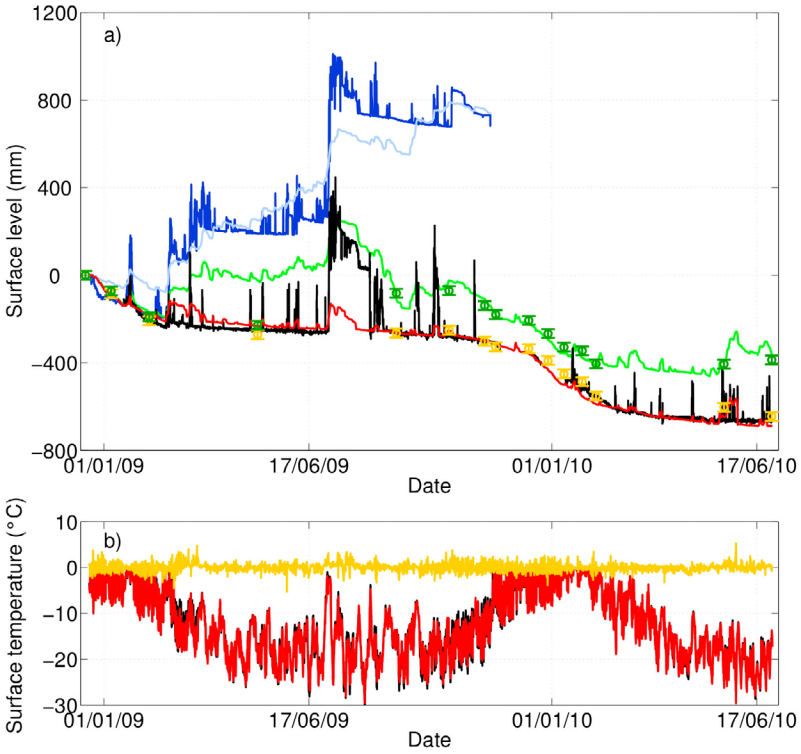

Figure 4. (a) Comparison of the modeled surface level for blue ice at BI-AWS (red line), for the 48-stake farm (light green line) and at D17 (light blue line). The measured surface elevation (black line) at BI-AWS and at D17 (dark blue line) were obtained from acoustic depth gauges. Orange dots are surface elevation measured at the closest stakes located in the blue ice area around BI-AWS. Dark green dots are surface elevation from an EOF analysis performed over the 48-stake farm measurements. Uncertainty bars are ±20 mm. (b) Comparison of measured (black line) and computed (red line) surface temperatures. The difference between measured and computed values is also shown (orange line).

its justification in direct density measurements, but ρ_{snow} is variable and depends on snow age. Full modeling of snow metamorphism (like in CROCUS) is clearly an important additional step for modeling permanent snow cover. Finally, the model mainly depends on two calibration parameters: R_{cyc} (which is linked to ρ_{snow}) and a_{ice}.

4.2. Energy Balance Model Validation

4.2.1. Modeling of Local Blue Ice Mass Balance

[38] Model results were compared with observations of surface elevation (Figure 4a), surface temperature (Figure 4b) and with measurements of ice temperature (at four levels) (Figure 5). The surface characteristics were well reproduced, with good timing of accumulation and erosion events. Differences between model and acoustic depth gauge measurement values were close to measurement uncertainties, except between 14 July 2009 and 6 September 2009, where measurements of snow depth suggest that accumulation was greater than in the model. Since summer sublimation was calibrated from direct measurements, sublimation is expected to be correctly modeled. Hence, the good agreement between measured and modeled ablation values suggests that melting was correctly computed.

[39] The mean modeled surface temperature was satisfactorily reproduced and was only 0.14°C lower than the mean measured temperature for the study period. This corresponds to a mean difference between modeled and measured outgoing long-wave radiation of 0.55 W m^{-2}, showing that the modeled surface heat budget was accurately computed. Temperature variations were also well reproduced (differences were generally $<\pm 1$°C with a standard deviation of 0.82°C). Despite the apparent discrepancy in modeled snow depth between 14 July 2009 and 6 September 2009, modeled and measured temperatures were similar. This suggests that surface characteristics under the pyrgeometer were correctly reproduced, because differences in surface roughness length would rapidly influence the surface heat budget and the modeled surface temperature. However, the modeled ice temperature was lower than observed temperature, because the modeled snow depth was underestimated in comparison with observations. This led to overestimation of ice cooling.

[40] Modeling the exact snow depth is crucial for SEB modeling. Assuming snow depth estimates from the acoustic depth gauge (SR50) led to a reduction in the discrepancies between modeled and measured surface temperature (mean difference was −0.05°C). However, the considerable increase in ice temperature after July 2009 was still underestimated. Modeling was only correct if snow depths (above the ice thermometers) between 14 July 2009 and 6 September 2009 were two times greater than below the SR50 acoustic depth gauge. These differences in snow depth under the sensors are not impossible because the thermometers were

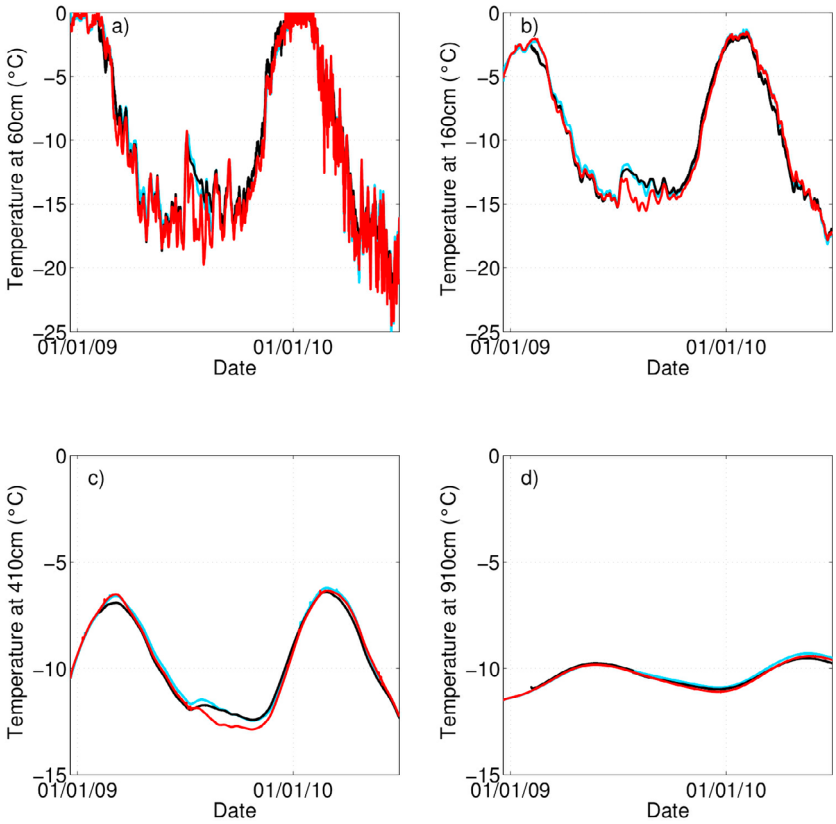

Figure 5. Comparison of the measured (black line) and computed (red line) ice temperature at depths of (a) 60 cm, (b) 160 cm, (c) 410 cm and (d) 910 cm. Also shown is modeled temperature assuming that snow depth is obtained with the acoustic depth gauge measurements (light blue line) and considering that snow depths above ice thermometers between 14 July 2009 and 6 September 2009 were 2 times greater than below the acoustic depth gauge.

installed 5 m away from the acoustic depth gauge and 8 m away from the pyrgeometer, and high sastrugis 40–50 cm in height were observed on stakes during this period (several stakes showed a snow depth of one meter whereas others showed uncovered ice).

4.2.2. Modeling the Mass Balance of the Mean 48-Stake Farm and at D17

[41] The model was tested to reproduce the mean net mass balance of the 48 stakes located around the station where the observed mass balance was only slightly negative (Figure 4). Modeling required $R_{cyc} = 0.99916$, leading to a 150 mm water equivalent (w.e.) (15%) lower net erosion than for BI-AWS. We also observed that the positive local accumulation at D17 station required a higher R_{cyc} value (R_{cyc} = 0.99945) leading to two times lower erosion efficiency than at BI. The low mean surface roughness length at D17 due to snow persistence also led to a reduction in sublimation.

4.3. Surface Heat Budget and Ablation Processes

[42] General features of the ablation processes (Figures 6 and 7) show that the meteorological variables (e.g., T, q and u) and the SEB are initially controlled by annual variations in incoming short-wave radiation. As the solar zenith angle increases, the SEB becomes more negative and the surface cools, and vice versa. Winter SEB was first characterized by almost zero $S_{\downarrow}$, and L was a central variable. Low $L_{\downarrow}$ led to low surface temperatures and $L_{\uparrow}$ values, which were crucial to balance the SEB (Figures 7a and 7b). The low surface temperatures induced very stable conditions and high θ^* values (Figure 7f), leading to high positive energy contribution to the surface by H (Figure 7d). Stable conditions in winter were associated with a slight strengthening of the katabatic wind. However, despite consistently high u^* values in winter, LE remained weak because cold air is a poor humidity reservoir and q^* remained close to zero in winter (Figure 7e) and $LE + H$ were positive (Figure 7c). Negative R (net radiation) values were only partly compensated by turbulent heat fluxes leading to marked cooling of the ice (Figure 5). After winter, as $S_{\downarrow}$ increased, the surface warmed leading to a reduction in stable conditions in the surface boundary layer (Figure 7f). The energy contribution was converted into turbulent heat fluxes [*Bintanja and van den Broeke*, 1995; *Wagnon et al.*, 2003] making R significantly correlated with LE + H (Figure 6b). Sublimation increased with the increase in air temperature. However, the negative contribution by LE + H was compensated by positive S values in summer, leading to ice warming and surface melting.

[43] Only low energy amounts (mean annual energy excess is 3 W m^{-2}) were available for melting. As also shown

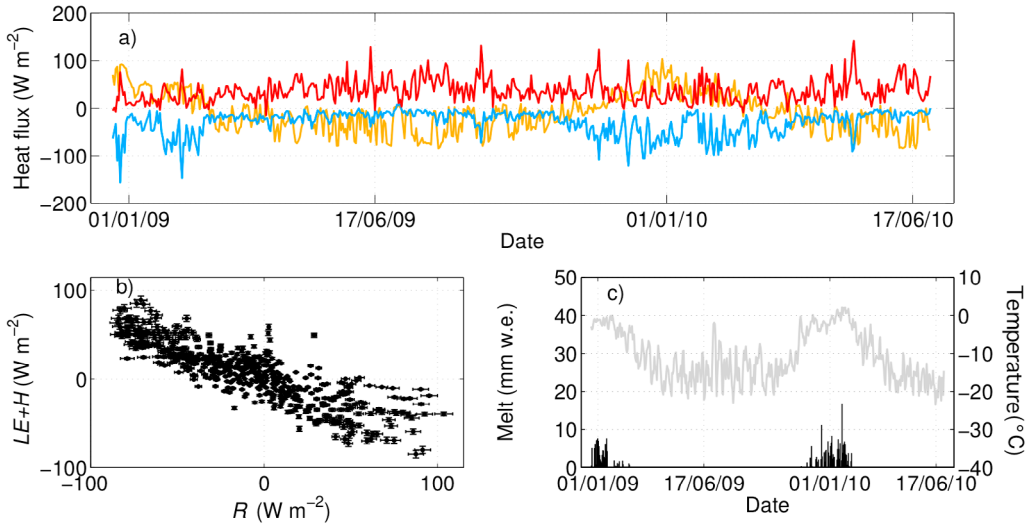

Figure 6. (a) Daily values of H (red line), LE (blue line) and R (orange line). (b) Comparison of daily net radiation (R) and daily turbulent heat flux sum (LE + H). Uncertainty bars are ±10%. (c) Comparison of daily melt (black bars) and daily temperature (gray line).

by *Genthon et al.* [2007], erosion was the largest ablation term. Over the cycle we studied, erosion was 1050 mm w.e., but sublimation (503 mm w.e.) and melting (280 mm w.e.) also played a crucial role in BI ablation processes. The accumulated melting and sublimation were concentrated in summer (Figure 6c). Hence, 100% of the accumulated melting was observed over a 6 month period (62% for sublimation). On the other hand, only 25% of erosion was observed

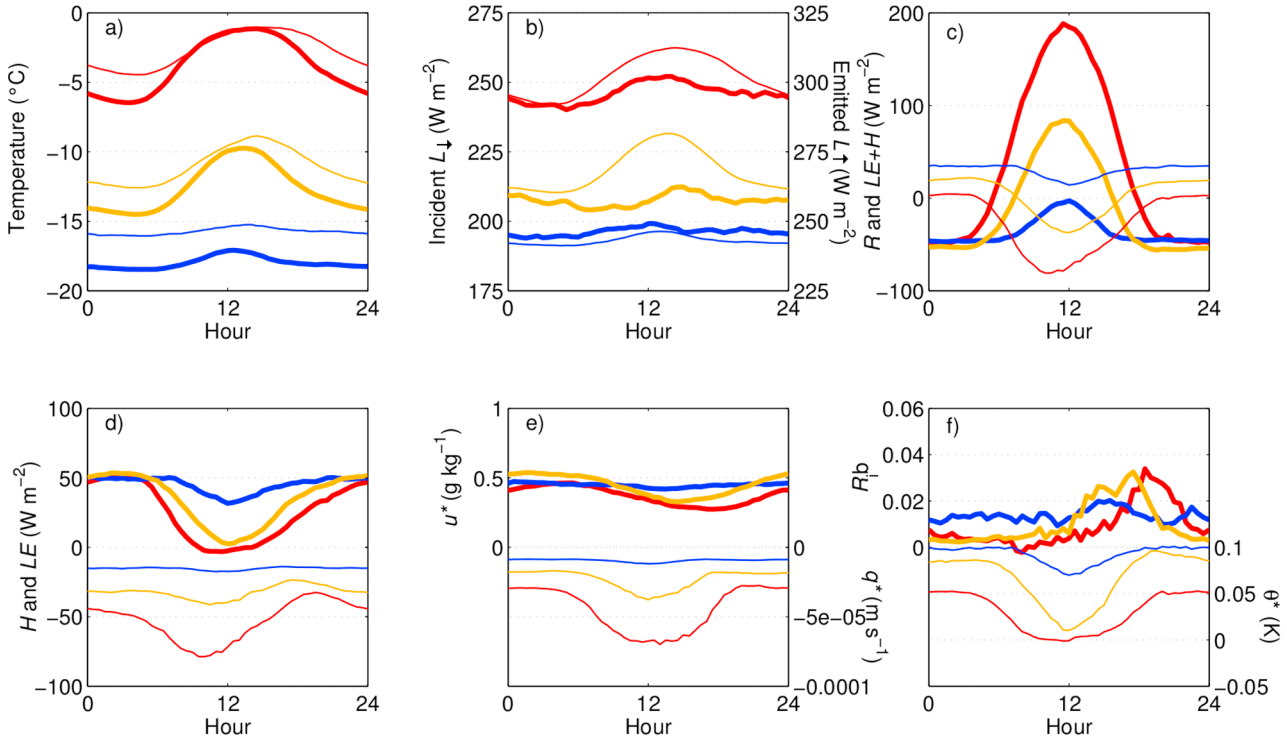

Figure 7. Mean diurnal cycle of meteorological and heat flux variables for (a) air temperature at a height of 2 m (narrow line) and surface temperature (thick line), (b) emitted (narrow line) and incoming longwave radiation (thick line), (c) turbulent heat fluxes LE + H (narrow lines) and net radiation (thick lines), (d) latent (narrow lines) and sensible (thick line) turbulent heat fluxes, (e) q* (narrow line) and u* (thick line), and (f) θ* (narrow line) and R_{ib} (thick line). Mean annual cycles are shown for summer (between 25 November and 25 February, red lines), winter (between 25 April and 25 September, blue lines), and intermediate seasons (remaining periods, orange lines).

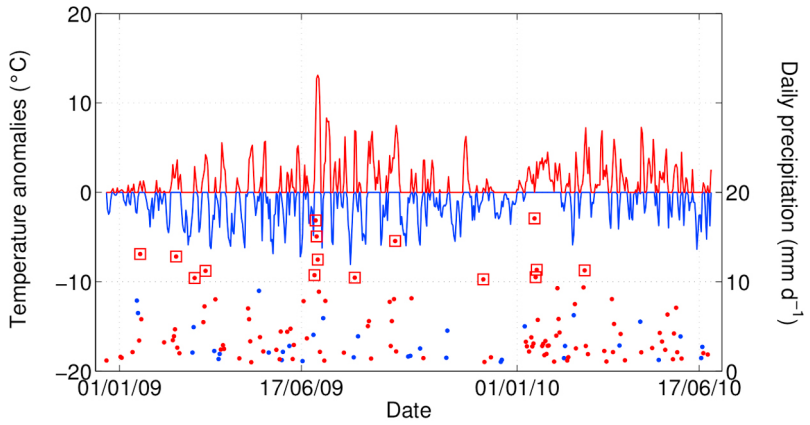

Figure 8. ERA-INTERIM daily precipitation (at 67°S, 140°E) on warm (red dots) and cold (blue dots) days. Small dots show when daily precipitation was greater than 1 mm d^{-1}, and large squares show when daily precipitation was greater than10 mm d^{-1}. The red line represents daily positive temperature anomalies, and the blue line represents the negative temperature anomalies.

during summer (the surface snow cover was not permanent in summer and erosion was reduced). $S_{\downarrow}$ and the surface albedo were crucial to explain the amount of summer melting. However, H and $L_{\downarrow}$ frequently acted as the main energy contributor to the surface, in agreement with the results of the sensitivity tests. The highest melting values occurred during warm events. The potential impact of these events on mass balance processes is discussed hereafter.

4.4. Warm Events

[44] Air temperature presented variations around a mean feature with a stable mean winter temperature (−14.8°C), a stable mean summer temperature (−1.3°C) and an almost linear decrease and increase during intermediate periods (Figure 2). Differences between temperature and the mean trend are hereafter referred to as temperature anomalies. Major positive temperature anomalies occur year round at BI-AWS. As already described in other areas of Antarctica [e.g., *van As et al.*, 2007], these warm air masses reflect depressions penetrating into the continent, and significant daily temperature increases observed at the coast also generally extend far inland (e.g., at Dome C, Figure 2).

[45] We observed that precipitation from ERA-Interim at (67.5°S, 140°E) was mainly associated with positive anomalies (Figure 8). Indeed, for the cycle concerned, ERA-Interim suggested the occurrence of 146 (14) events in which daily precipitation exceeded 1 mm w.e. d^{-1} (10 mm w.e. d^{-1}). Of these events, 83% (100%) occurred during positive temperature anomalies. On the other hand, cold situations were not associated with snow precipitation, because they were mainly due to cold descending katabatic winds. The largest precipitation events occurred during very warm periods. For instance, the highest temperature values observed in winter and in summer were both associated with very intense precipitation (between 30 May 2009 and 6 July 2009 and during the second half of January 2010).

[46] The intrusion of a depression was coupled with high H and $L_{\downarrow}$ values leading to an abrupt change in the surface energy contribution [e.g., *van As et al.*, 2007]. Major increases in surface and ice temperature at BI-AWS in winter reflected this change. In summer, warm events led to the highest melting rates observed at BI-AWS during the study period. However, there were major differences between low elevation BI areas and positive mass balance areas inland because melting was reduced at higher elevations (e.g., at D17) and snow accumulated despite the high temperatures.

5. Discussion and Conclusion

[47] In Cap Prudhomme area, BI is only observed in a 1 km belt close to the sea shore [*Agosta et al.*, 2011] where high erosion caused by the wind, high sublimation, and melting combine to produce negative mass balances [e.g., *Bintanja et al.*, 1997; *Genthon et al.*, 2007]. Erosion at BI-AWS is very high compared to that in surrounding areas, where a positive net accumulation is observed. For instance, lower erosion was observed at D17 than at BI-AWS, even if the mean annual wind speed was higher at D17 (8.9 m s^{-1} compared to 8.4 m s^{-1} at BI-AWS). Using the BI-AWS R_{cyc} parameter value would lead to marked ablation at D17. Erosion at D17 clearly suggests that the airflow is more convergent than at the coast. However, the D17 site, and to lesser extent the upper part of the 48-stake farm, are both located leeward from snow covered areas, whereas BI area is located leeward from high ice cliffs above the sea (Figure 1). We suppose that part of the eroded snow upstream drifts and is deposited at D17 leading to more efficient sedimentation processes. Snow accumulation indirectly impacts albedo values and causes a reduction in summer melting.

[48] Runoff occurs in BI areas at Cap Prudhomme. We observed that melting increased considerably during warm events. What would happen if warm events were more frequent and more intense? Because GCMs currently suggest that precipitation would increase in a warmer climate [e.g., *Krinner et al.*, 2007], we performed a sensitivity test on the mass balance for precipitation and temperature increases. We computed the SEB with 10% more precipitation than that given by ERA-Interim. At BI-AWS, modeling showed that the mass balance would be compensated if 0.1°C warming occurred. Actually, high erosion at the BI site currently pre-

vents snow from accumulating and an increase in precipitation would only slightly affect the BI area. On the other hand, for the 48-stake farm, we observed that an increase of 1.5°C would be necessary to compensate a 10% more precipitation. This situation suggests that an increase in precipitation would lead to a more positive surface mass balance except in BI areas. Hence, despite the fact GCM did not consider erosion [e.g., *Krinner et al.*, 2007], mass balance forecasts suggesting an increase in accumulation are likely to be correct.

[49] However, erosion processes clearly depend on the spatial characteristics of the terrain (mounts, surface depressions), and assessing the spatial distribution of the mass balance at a regional scale requires distributed modeling. For instance, according to GLACIOCLIM stake line measurements made in the first 150 km inland [*Agosta et al.*, 2011], the mass balance presents extreme variability at the kilometer and mesoscale in the first 150 km from the coast. Even if higher melting and sublimation values are observed close to the coast, these processes alone cannot explain the observed spatial pattern of net accumulation, and erosion must thus play an important role in this distribution. To date, erosion and snowdrift in Antarctica has only been modeled by MAR and RACMO2 models. Climate models currently do not provide information at very high resolution. An important large scale study is currently underway on accumulation regionalization. Implementation of erosion processes is a key step in this work.

[50] Finally, erosion modeling requires good input data that reflect the coincidence between wind and precipitation [*Genthon et al.*, 2007]. Our good quality modeling results from the relevance of ERA-Interim precipitation in terms of timing and amounts at a daily time scale. *Agosta et al.* [2011] also suggested that the mean regional mass balance and its interannual variations are well reproduced by ECMWF in the Cap Prudhomme area. Obtaining long-term data for model validation is also crucial to assess model quality. The GLACIOCLIM-SAMBA observatory was set up with this aim in view and more data will be collected and distributed on the Internet for use by the wider community.

[51] **Acknowledgments.** GLACIOCLIM-SAMBA observatory is supported by IPEV and INSU. Some of the instruments were funded by IPEV programs (CONCORDIASI and CALVA programs) and by the European Union FP7 program ICE2SEA. We are also extremely grateful to IPEV for their logistical support in the field, and particularly recall Anthony Mangel and Frédéric Vuillaume, who gave their lives to providing logistical support for Antarctic Research. Finally, we thank D. van As, M. Truffer and one anonymous reviewer for their valuable comments.

References

Agosta, C., V. Favier, C. Genthon, H. Gallée, G. Krinner, J. T. Lenaerts, and M. R. van den Broeke (2011), A new surface accumulation dataset for Adelie Land, Antarctica (66°S, 139°E): Application for model validation, *Clim. Dyn.*, doi: 10.1007/s00382-011-1103-4, in press.

Ambach, W. (1974), The influence of cloudiness on the net radiation balance of a snow surface with high albedo, *J. Glaciol.*, *13*(67), 73–84.

Andreas, E. L. (1987), A theory for scalar roughness and the scalar transfer coefficient over snow and sea ice, *Boundary Layer Meteorol.*, *38*, 159–184, doi:10.1007/BF00121562.

Ångström, A. (1961), Techniques of determining the turbidity of the atmosphere, *Tellus*, *13*(2), 214–223, doi:10.1111/j.2153-3490.1961.tb00078.x.

Bintanja, R. (1999), On the glaciological, meteorological, and climatological significance of Antarctic blue ice areas, *Rev. Geophys.*, *37*(3), 337–359, doi:10.1029/1999RG900007.

Bintanja, R., and M. R. van den Broeke (1995), The surface energy balance of Antarctic snow and blue ice, *J. Appl. Meteorol.*, *34*(4), 902–926, doi:10.1175/1520-0450(1995)034<0902:TSEBOA>2.0.CO;2.

Bintanja, R., S. Jonsson, and W. Knap (1997), The annual cycle of the surface energy balance of Antarctic blue ice, *J. Geophys. Res.*, *102*(D2), 1867–1881, doi:10.1029/96JD01801.

Bird, R. E., and R. L. Hulstrom (1981), A simplified clear sky model for direct and diffuse insolation on horizontal surfaces, *Tech. Rep. SERI/TR-62-761*, Sol. Res. Inst., Golden, Colo.

Bourges, B. (1985), Improvement in solar declination computation, *Sol. Energy*, *35*(4), 367–369, doi:10.1016/0038-092X(85)90144-6.

Corripio, J. G. (2003), Modelling the energy balance of high altitude glacierised basins in the Central Andes, Ph.D. Thesis, Univ. of Edinburgh, Edinburgh, U. K.

Denby, B., and W. Greuell (2000), The use of bulk and profile methods for determining surface heat fluxes in the presence of glacier winds, *J. Glaciol.*, *46*(154), 445–452, doi:10.3189/172756500781833124.

Dorsey, N. E. (1940), *Properties of Ordinary Water-Substance in All Its Phases: Water-Vapor, Water, and All the Ices*, Reinhold, New York.

Douville, H., J. F. Royer, and J. F. Mahfouf (1995), A new snow parameterization for the Météo-France climate model, Part I: Validation in stand-alone experiments, *Clim. Dyn.*, *12*, 21–35, doi:10.1007/BF00208760.

Eisen, O., et al. (2008), Ground-based measurements of spatial and temporal variability of snow accumulation in East Antarctica, *Rev. Geophys.*, *46*, RG2001, doi:10.1029/2006RG000218.

Favier, V., P. Wagnon, J.-P. Chazarin, L. Maisincho, and A. Coudrain (2004), One-year measurements of surface heat budget on the ablation zone of Antizana Glacier 15, Ecuadorian Andes, *J. Geophys. Res.*, *109*, D18105, doi:10.1029/2003JD004359.

Gallée, H., and P. Pettré (1998), Dynamical constraints on katabatic wind cessation in Adélie Land, Antarctica, *J. Atmos. Sci.*, *55*, 1755–1770, doi:10.1175/1520-0469(1998)055<1755:DCOKWC>2.0.CO;2.

Gallée, H., G. Guyomarc'h, and E. Brun (2001), Impact of snow drift on the Antarctic Ice Sheet surface mass balance: Possible sensitivity to snow-surface properties, *Boundary Layer Meteorol.*, *99*(1), 1–19, doi:10.1023/A:1018776422809.

Gallée, H., C. Agosta, L. Gential, V. Favier, and G. Krinner (2011), A downscaling approach towards high-resolution surface mass balance over Antarctica, *Surv. Geophys.*, doi: 10.1007/s10712-011-9125-3, in press.

Gallet, J. C. (2010), La neige du plateau antarctique: Surface spécifique et applications, Ph.D. thesis, 148 pp., Univ. Joseph Fourier, Grenoble, France.

Genthon, C., P. Lardeux, and G. Krinner (2007), The surface accumulation and ablation of a blue ice area near Cap Prudhomme, Adélie Land, Antarctica, *J. Glaciol.*, *53*(183), 635–645, doi:10.3189/002214307784409333.

Georges, C., and G. Kaser (2002), Ventilated and unventilated air temperature measurements for glacier-climate studies on a tropical high mountain site, *J. Geophys. Res.*, *107*(D24), 4775, doi:10.1029/2002JD002503.

Helsen, M. M., M. R. van den Broeke, R. S. W. van de Wal, W. J. van de Berg, E. van Meijgaard, C. H. Davis, Y. Li, and I. Goodwin (2008), Elevation changes in Antarctica mainly determined by accumulation variability, *Science*, *320*(5883), 1626–1629, doi:10.1126/science.1153894.

Hock, R., and B. Holmgren (2005), A distributed surface energy-balance model for complex topography and its application to Storglaciären, Sweden, *J. Glaciol.*, *51*(172), 25–36, doi:10.3189/172756505781829566.

Hoffman, M. J., A. G. Fountain, and G. E. Liston (2008), Surface energy balance and melt thresholds over 11 years at Taylor Glacier, Antarctica, *J. Geophys. Res.*, *113*, F04014, doi:10.1029/2008JF001029.

Intergovernmental Panel on Climate Change (2007), *Climate Change 2007: The Physical Science Basis. Contribution of Working Group I to the Fourth Assessment Report of the Intergovernmental Panel on Climate Change*, edited by S. Solomon et al., Cambridge Univ. Press, Cambridge, U. K.

Iqbal, M. (1983), *An Introduction to Solar Radiation*, Academic, Toronto, Ont., Canada.

King, J. C., and J. Turner (1997), *Antarctic Meteorology and Climatology*, Cambridge Univ. Press, Cambridge, U. K., doi:10.1017/CBO9780511524967.

König-Langlo, G., J. C. King, and P. Pettre (1998), Climatology of the three coastal Antarctic stations Dumont d'Urville, Neumayer, and Halley, *J. Geophys. Res.*, *103*(D9), 10,935–10,946, doi:10.1029/97JD00527.

Korona, J., E. Berthier, M. Bernard, F. Rémy, and E. Thouvenot (2009), SPIRIT. SPOT 5 stereoscopic survey of polar ice: Reference images and topographies during the fourth International Polar Year (2007–2009), *ISPRS J. Photogramm. Remote Sens.*, *64*, 204–212, doi:10.1016/j.isprsjprs.2008.10.005.

Krinner, G., O. Magand, I. Simmonds, C. Genthon, and J. Dufresne (2007), Simulated Antarctic precipitation and surface mass balance at the end of

the twentieth and twenty-first centuries, *Clim. Dyn.*, *28*(2–3), 215–230, doi:10.1007/s00382-006-0177-x.

Monaghan, A. J., et al. (2006), Insignificant change in Antarctic snowfall since the International Geophysical Year, *Science*, *313*(5788), 827–831, doi:10.1126/science.1128243.

Niemelä, S., P. Räisänen, and H. Savijärvi (2001), Comparison of surface radiative flux parameterizations. Part II: Shortwave radiation, *Atmos. Res.*, *58*, 141–154, doi:10.1016/S0169-8095(01)00085-0.

Obleitner, F., and J. de Wolde (1999), On intercomparison of instruments used within the Vatnajökull glacio-meteorological experiment, *Boundary Layer Meteorol.*, *92*, 25–35, doi:10.1023/A:1002074627334.

Oke, T. R. (1987), *Boundary Layer Climates*, 2nd ed., 435 pp., Routledge, New York.

Picard, G., L. Brucker, M. Fily, H. Gallée, and G. Krinner (2009), Modeling time series of microwave brightness temperature in Antarctica, *J. Glaciol.*, *55*(191), 537–551, doi:10.3189/002214309788816678.

Pirazzini, R. (2004), Surface albedo measurements over Antarctic sites in summer, *J. Geophys. Res.*, *109*, D20118, doi:10.1029/2004JD004617.

Rasmus, K. (2009), A thermo-hydrodynamic modelling study of an idealized low-elevation blue-ice area in Antarctica, *J. Glaciol.*, *55*(194), 1083–1091, doi:10.3189/002214309790794805.

Reijmer, C. H., R. Bintanja, and W. Greuell (2001), Surface albedo measurements over snow and blue ice in thematic mapper bands 2 and 4 in Dronning Maud Land, Antarctica, *J. Geophys. Res.*, *106*, 9661–9672, doi:10.1029/2000JD900718.

Rignot, E., J. L. Bamber, M. R. van den Broeke, C. Davis, Y. Li, W. J. van de Berg, and E. van Meijgaard (2008), Recent Antarctic ice mass loss from radar interferometry and regional climate modelling, *Nat. Geosci.*, *1*(2), 106–110, doi:10.1038/ngeo102.

Simmons, A., S. Uppala, D. Dee, and S. Kobayashi (2006), ERA-Interim: New ECMWF reanalysis products from 1989 onwards, *ECMWF Newsl.*, *110*, 25–35.

Smeets, C. J. P. P., and M. R. van den Broeke (2008), The parameterisation of scalar transfer over rough ice, *Boundary Layer Meteorol.*, *128*, 339–355, doi:10.1007/s10546-008-9292-z.

van As, D., M. R. van den Broeke, and M. M. Helsen (2007), Strong wind events and their impact on the near surface climate at Kohnen Station on the Antarctic Plateau, *Antarct. Sci.*, *19*(04), 507–519, doi:10.1017/S095410200700065X.

van den Broeke, M. R., D. van As, C. Reijmer, and R. van de Wal (2005), Sensible heat exchange at the Antarctic snow surface: A study with automatic weather stations, *Int. J. Climatol.*, *25*(8), 1081–1101, doi:10.1002/joc.1152.

van den Broeke, M., W. J. van de Berg, E. van Meijgaard, and C. Reijmer (2006), Identification of Antarctic ablation areas using a regional climate model, *J. Geophys. Res.*, *111*, D18110, doi:10.1029/2006JD007127.

Wagnon, P., J.-E. Sicart, E. Berthier, and J.-P. Chazarin (2003), Wintertime high-altitude surface energy balance of a Bolivian glacier, Illimani, 6340 m above sea level, *J. Geophys. Res.*, *108*(D6), 4177, doi:10.1029/2002JD002088.

Wendler, G., and N. Ishikawa (1988), Measurements of the atmospheric turbidity at D47, Adelie Land, a contribution to I.A.G.O, *Polarforshung*, *58*(1), 41–46.

C. Agosta, L. Arnaud, V. Favier, H. Gallée, and C. Genthon, LGGE, UJF-CNRS, 54 rue Molière, BP 96, F-38402 Saint Martin d'Hères, France. (favier@lgge.obs.ujf-grenoble.fr)

A. Trouvillez, Cemagref, UR ETNA, 2 rue de la Papeterie, BP 76, F-38402 Saint Martin d'Hères, France.